Helium implantation damage resistance in nanocrystalline W-Ta-V-Cr high entropy alloys

O. El-Atwani [a, *], A. Alvarado [b], K. Unal [a], S. Fensin [a], J.A. Hinks [c], G. Greaves [c], J.K.S. Baldwin [d], S.A. Maloy [a], E. Martinez [b]

[a] Materials Science and Technology Division, Los Alamos National Laboratory, Los Alamos, NM, 87545, USA
[b] Theoretical Division, Los Alamos National Laboratory, Los Alamos, NM, 87545, USA
[c] School of Computing and Engineering, University of Huddersfield, HD1 3DH, UK
[d] Center for Integrated Nanotechnologies, MPA-CINT, Los Alamos National Laboratory, Los Alamos, NM, 87545, USA

ARTICLE INFO

ABSTRACT

Nanocrystalline W-Ta-Cr-V high entropy alloys have shown promising properties as nuclear fusion materials with enhanced radiation resistance to heavy ion irradiation and negligible radiation hardening. In this work, we investigate the performance of the alloy under low energy helium (He) implantation up to a fluence of 1.25×10^{17} cm^{-2} at 1223 K. We observe a uniform high density of very small (~2–3 nm) bubbles grown at a slow rate along with enhanced He bubble damage resistance, further marked by no preferential bubble formation on the grain boundaries, even at much higher fluences compared to previously implanted tungsten grades. First principle calculations of He formation and migration energies in this alloy indicate deep energetic wells on the potential landscape and low diffusivity of He compared to pure W. The results imply higher overall (considering both grain matrices and grain boundaries) implantation resistance due to slow He diffusion and accumulation, and confirm the enhanced vacancy-self interstitial recombination argument in these alloys.

Crown Copyright © 2020 Published by Elsevier Ltd. All rights reserved.

1. Introduction

Harvesting energy from controlled fusion reactions poses one of the most significant challenges for mankind [1–5]. Environmentally benign and effectively limitless, this form of power generation could potentially meet the continuously growing energy demand worldwide. Important issues in both plasma stability and confinement along with material performance remain to be solved. The deuterium (D)-tritium (T) plasma generates large amounts of energetic neutrons and helium (He) ash that ultimately collide with functional or structural materials, including the divertor and first wall, depositing energy (heat), causing surface-atom removal and redeposition many times over within an operational year [6]. Hence, high fluxes of low energy particles (~10^{22} m^{-2}.s^{-1}) reach the surface, leading to material erosion that may contaminate the plasma, generating deleterious instabilities that might produce critical component damage [7]. Fast neutrons (~10^{18} m^{-2}.s^{-1}) pose a similar threat to the entire reactor structure, producing up to

several hundreds of atomic displacements per atom (dpa) over a component lifetime with concurrent transmutation of solid atoms, producing percent levels of H and He [8]. Ultra-high, time-dependent heat fluxes during normal operation (~10 MW.m^{-2}) reaching several GW.m^{-2} in plasma disruptions impose thermomechanical demands on large, complex and intricate structures that are also totally unprecedented and may present an immense challenge [9]. Thus, maintaining the structural integrity of components under such a radical nonequilibrium set of conditions, as well as plasma stability, is a fundamental feasibility issue for fusion energy.

Tungsten (W) is the leading candidate for plasma-facing components due to its high melting temperature, good thermal conductivity, low sputter yield and low tritium retention [10]. However, under irradiation, W suffers severe microstructural changes [11–14] that can eventually modify the thermal and mechanical properties of the material.

To mitigate these drawbacks, we have recently developed a refractory high entropy alloy (HEA) with atomic composition around W35%-Ta35%-V15%-Cr15% of single BCC phase that shows outstanding radiation resistance and thermal stability to grain growth under heavy ion irradiation at 1073 K [15]. HEAs are

mixtures of several principal elements that can show improved properties for structural and functional applications [16–18]. Some of these HEAs are being studied for nuclear applications [19]. In this context, the chemical heterogeneity leads to disordered states in the electronic structure that generally results in enhanced electron sputtering, reducing the electronic and thermal conductivities [20,21]. Such reduced conductivities lead to energy localization that enhances defect recombination. Chemical heterogeneity also leads to rough energy landscapes that modify the long-range transport properties of irradiation-created defects [22]. The goal would be to optimize the landscape to promote defect recombination over clustering formation, such that irradiation does not dramatically modify the materials properties.

As mentioned above, large amounts of He implantation from the plasma ash constitute a big concern in plasma-facing materials. The purpose of this paper is to test the response of the W-based HEA upon He implantation. We combine experiments and modeling to understand the basic properties of interstitial He in the material and the long-term microstructural evolution in terms of bubble size and density distributions.

2. Material and methods

The sample implanted was a thin 100 nm thickness foil prepared by magnetron deposition on top of NaCl salt before being floated on to a TEM molybdenum grid. The implantation experiment was performed *in-situ* within the transmission electron microscope (TEM) in the MIAMI-2 system (Microscope and Ion Accelerators for Materials Investigations) at the University of Huddersfield [23]. The implantation was performed with 2 keV He ions at 18.7° from the surface normal with a flux of 8.8×10^{13} cm^{-2}.s^{-1}, to a total He$^+$ fluence of 1.65×10^{17} cm^{-2}. The sample temperature during implantation was 1223 K. Ion and damage distributions from implantation are shown in the supplemental material using both "Kinchin-Pease" (Fig. S1) and "Detailed Calculation and Full Damage Cascade" (Fig. S2) options in the Stopping and Range of Ions in Matter (SRIM) Monte Carlo computer code (version 2013) [24] using 40 eV as a displacement threshold for all elements [25]. Bubble formation, distribution, and evolution in the materials were studied by quantifying bubble density, average size and total change in volume (in the grain matrices of the material due to bubble formation) as a function of implantation He$^+$ fluence. The methodology involved in bubble damage quantification is described in detail in Ref. [26]. The morphology of the sample was demonstrated to consist of a bimodal grain size distribution with ~70% of the grains in the nanocrystalline regime ($\leq$100 nm) and the remaining in the ultrafine (100−500 nm) with an underlying single BCC phase and compositional striations in the individual grains that are stable at high temperatures [15].

3. Theory

We used electronic structure calculations as implemented in the VASP code to compute formation and migration energies of He in the tetrahedral and octahedral sites of $4 \times 4 \times 4$ BCC supercells with 128 atoms. We have used projector augmented wave pseudopotentials and exchange-correlation interactions described by the generalized gradient approximation of the Perdew-Burke-Ernzerhof form. We employed a Methfessel-Paxton smearing with width 0.2 eV and periodic boundary conditions in all directions with a cutoff energy of plane waves of 350 eV. The Brillouin zone was sampled in a $3 \times 3 \times 3$ k-point mesh with a Monkhorst-Pack scheme. The convergence threshold for the total energy and atomic force were 10^{-4} eV and 10^{-2} eV.Å^{-1}, respectively. We did not consider spin polarization in this study, since its effect in the results

was minimal. We have generated a total of 45 random configurations with the average composition matching the experimental values, and we have minimized the energy of the system at zero pressure and temperature, first without He, and computed the formation energy per atom:

$$E_f = \frac{\left\{ E[HEA] - \sum_{i=1}^{4} N_i E_i^{ref} \right\}}{N} \tag{1}$$

where $E[HEA]$ is the energy of the system as given by *ab initio*, N, N_i and E_i^{ref} are the total number of atoms, number of atoms type i and reference energy of atom type i, respectively. The reference energies, E_i^{ref}, are −12.970, −11.824, −9.645 and −9.067 eV for W, Ta, Cr and V, respectively. The concentrations probed were 36.16 ± 0.96 at.% for W, 36.22 ± 0.96 at.% for Ta, 15.07 ± 0.96 at.% for Cr and 12.53 ± 0.89 at.% for V.

In these structures we have introduced interstitial He in different tetrahedral and octahedral sites for a total of 163 different configurations, and we have again relaxed the system at zero pressure and temperature. We have computed the formation energy similarly:

$$E_f = E[HEA + He] - \sum_{i=1}^{5} N_i E_i^{ref} \tag{2}$$

using a reference energy for the He, $E_{He}^{ref} = -0.133$ eV in an FCC lattice. We have also computed the solution energy, defined as:

$$E_s = E[HEA + He] - E[HEA] - E_{He}^{ref} \tag{3}$$

4. Results

The implantation was performed at similar conditions to previous studies on pure W grades and an ultrafine W-TiC alloy [27,28], such that a meaningful comparison between the performance of this HEA and those works is possible. Fig. 1 shows the bright-field images of a small implanted region at different fluences. Uniform small bubble formation is shown across all grains and grain boundaries. Although vacancies created during implantation preferentially form He-vacancy complexes [29], which lead to excess interstitial defects, large loop formation did not occur even at a peak dpa of ~6.3 dpa from Kinchin-Pease model calculations; the peak dpa value jumps to 17 dpa if "Detailed Calculation with full Damage Cascade" option is used. This contradicts previous works on pure nanocrystalline W and ultrafine W-TiC alloys where formation of large loops, loop interaction, coalescence and dislocation formation occurred at peak dpa of less than 1 dpa [27,30]. The W-based HEA previously demonstrated outstanding loop formation resistance under heavy ion irradiation [15] unlike pure W and conventional W alloys, which were prone to dislocation loop formation and loop rafting [31]. It is also important to mention that the absence of black dot formation in the HEA indicates that the compositional striations observed in this alloy after deposition are still preserved unlike in the heavy ion irradiation case [15] where Cr and V segregation occurred and the compositional striations are lost. Quantification of the small bubble damage is shown in Fig. 2. Bubble density, areal size and the commonly used correlation between cavity population and estimated volumetric swelling (found using $\Delta v/_v = \frac{4}{3}\pi r_c^3 N_v$ where N_v is the bubble density in the 100 nm thick foil and r_c is the average radius of the bubbles) are plotted. Bubble density is shown to increase and peak at a fluence of
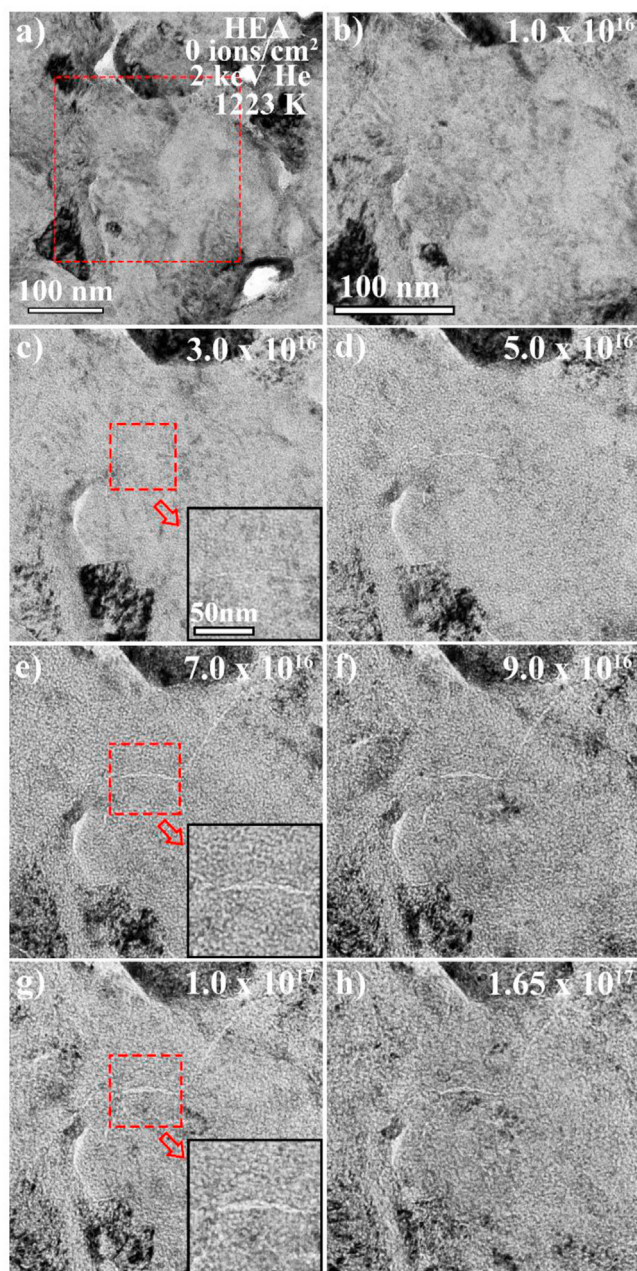
Fig. 1. a−h: Bright-field TEM micrographs of a small implanted region taken under Fresnel conditions (under-focused) showing He bubble formation and evolution as a function of He+ fluence in the grain matrices and grain boundaries implanted *in-situ* with 2 keV He+ at 1223 K. Scale bar of **b−h** is the same and is shown in **b**. Red box in **a** approximately represents a magnified region presented in **b** to **h**. Insets in **c, e** and **g** show a magnified portion of the same grain boundary (scale bar is shown in **c**).

Fig. 2. Helium bubble density, average area and the total change in volume in the grain matrices as a function of He+ implantation fluence. (For interpretation of the references to color in this figure legend, the reader is referred to the web version of this article.)

2.5×10^{16} cm^{-2} before it decreases and plateaus (after a fluence of ~1.0×10^{17} cm^{-2}). Bubble sizes increase slowly as a function of time and plateaus at ~1.0×10^{17} cm^{-2}, while change in volume increases rapidly up to the fluence of ~2.5×10^{16} cm^{-2} and also reaching a plateau at ~1.0×10^{17} cm^{-2}. Elucidating the plateauing of the total damage needs further detailed work and is a topic of future research in these HEAs. It should be noted that the surface proximity effect (due to low implantation depth of He at 2 keV) can affect bubble formation, defect annihilation and recombination. However, this effect decreases significantly in nanocrystalline microstructures when the grain boundary to surface ratio is close or
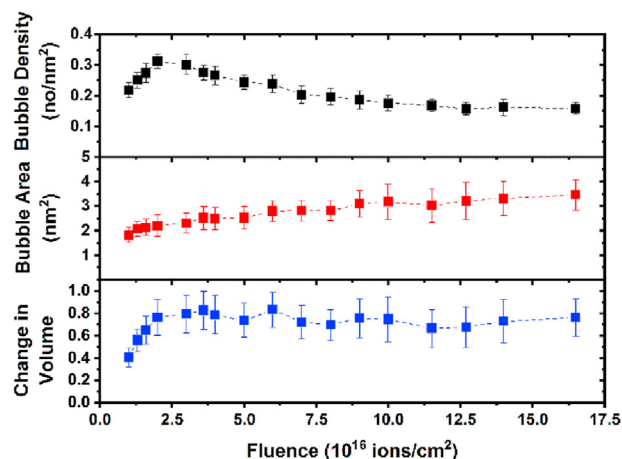
exceeds the value of 1 [32]. Moreover, this effect should accelerate bubble formation and enhance bubble damage due to interstitial migration to the surfaces, but bubble damage in the HEA is still remarkably small. The bubble damage in the HEA, after bubble nucleation, stems from an increase in size rather than new bubble nucleation. This is manifested in Fig. 2 where density saturates while bubble size continues to increase. Furthermore, from the histograms in Fig. 3, it is clearly seen that there is a shift from small to larger sizes as fluence increases. The damage is then attributed to an increase in the He content rather than long-range defect transport.

When compared to previously reported results on pure nanocrystalline W (average grain size of ~85 nm) and ultrafine W-TiC alloys (average grain size of ~290 nm) [27], the bubble density at a fluence of 3.5×10^{16} cm^{-2} in bulk is ~100 and 35 times larger in the HEA than in the W-TiC and magnetron deposited nanocrystalline W materials, respectively. It is also larger than in pure nanocrystalline and ultrafine grained W (grain size of 60−400 nm) formed by severe plastic deformation (SPD W) [28]. The bubble size, however, is smaller. The overall change in bulk volume is about 1.3 and 2.0 times larger than in W-TiC and magnetron deposited W, respectively. At this fluence, larger changes in bubble damage occurred at the grain boundaries relative to the grain matrices in the nanocrystalline W and the W-TiC grades. At the same fluence, bubble damage in the HEA is near its maximum (bubble density also peaks at a fluence of around 2.3×10^{16} cm^{-2}). At the fluence where bubble damage reached a plateau in the HEA, the overall change in volume is similar to the W-TiC and 1.5 times the nanocrystalline deposited W. It could then be assumed that the performance of this HEA is similar to the other nanocrystalline grades and conventional ultrafine alloys. However, this damage quantification takes into account only the bubbles in the grain matrices (which can be counted and quantified). Still, bubbles on the grain boundaries also contribute to the change in volume. Unfortunately, bubble damage quantification on the grain boundaries is not possible with edge-on grain boundaries since bubble density and size vary as a function of grain boundary angle and plane. In the magnetron deposited nanocrystalline W, the SPD W and the W-TiC alloy, preferential bubble formation on the grain boundaries occurs, with large bubble density and size distributions [27,28]. Preferential bubble formation at the grain boundaries has been linked to mechanical property degradation and overall larger swelling [33,34].
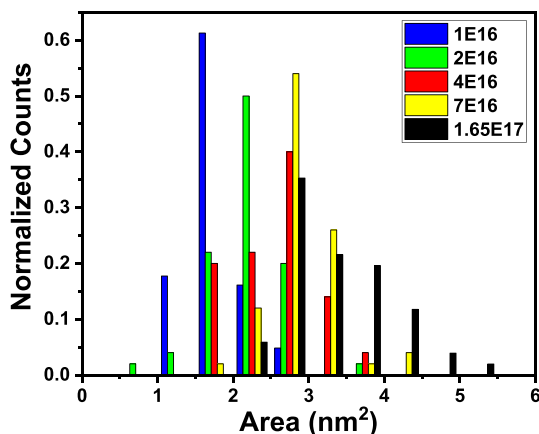
Fig. 3. Normalized bar graphs of bubble size distributions in the grain matrices in the HEA as a function of implantation He⁺ fluence. (For interpretation of the references to color in this figure legend, the reader is referred to the web version of this article.)

The large preferential He bubble formation on the grain boundaries in the magnetron deposition W, the SPD W and the W-TiC was observed using TEM with 8−10 nm, 10 nm and 20−25 nm average bubble sizes, respectively [27,28]. These bubbles were shown to reach large sizes even at fluences as low as ~3.5 × 10^{15} cm^{-2}. These bubbles form due to the effect of high grain boundary density, in ultrafine and nanocrystalline materials, in absorbing high defect (vacancies and He-vacancy clusters) populations and trapping He particles. On the other hand, no large preferential He bubble formation occurred on the grain boundaries in the HEA (Fig. 1) even at over one order of magnitude larger fluence. Using inclined grain boundaries where bubble density can be determined (in addition to size), the total change in volume, bubble size and the corresponding change in volume on the grain boundaries of fine-grained W were shown to continuously increase and to be ~5 times larger than the grain matrices. In the HEA, this is not the case and bubbles are uniformly distributed, with no preferential segregation to GBs. Therefore, the total He bubble damage in the HEA is significantly lower compared to the above-mentioned materials. Since fuzz formation has been correlated to a high density of He bubbles, we expect fuzz to occur in these HEAs at much higher fluences than in SPD W, which in turn was shown to happen at an order of magnitude higher fluence compared to coarse grained W. Moreover, the softening effect observed in SPD W [33] is also expected to vanish as it was related to He bubble segregation to GBs.
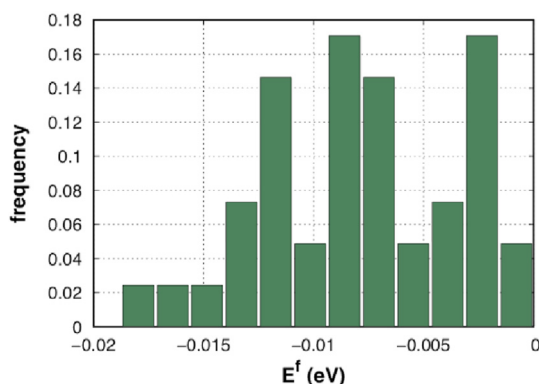
On the modeling side, all the values that we have obtained for the formation energies of these alloys are negative (see Fig. 4). In binary systems, a negative enthalpy of mixing is usually related to an ordering tendency. However, in HEAs, with more degrees of freedom, the competition between different elements makes it harder to predict what kind of ordering might happen. The average result is −7.89 meV per atom with standard deviation $\sigma = 4.29$ meV per atom.

In the samples containing He, we observe that the equilibrium site for the He atom is displaced from purely tetrahedral or octahedral sites. In these alloys, with large lattice distortions, the unit cells lose their symmetry and the interstitial sites also become distorted. An example of the equilibrium position of an interstitial He is shown in Fig. 5b.

We have computed the distribution of distances between the He and its atomic neighbors up to a radius of 2.5 Å, which encompasses both tetrahedral and octahedral sites. The results are shown in Fig. 5a. We observe two peaks, the first one at around 1.7 Å and the second at 1.9 Å, which would correspond to octahedral and tetrahedral sites. However, the distribution is broad indicating that the He tends to delocalize leading to symmetry-broken configurations. Hence, we have computed the formation energies of interstitial He in its relaxed configurations following Eq. (2). Fig. 6a shows the distribution of values obtained. We note that the data follows closely a Gaussian distribution $\mathscr{N}(\mu, \sigma^2) = {1}/{\sigma\sqrt{2\pi}} exp\left(-\frac{1}{2}\frac{(E_f - \mu)^2}{\sigma^2}\right)$, with average $\mu = 3.57$ eV and standard deviation $\sigma = 0.86$ eV.

The resulting distribution for the solution energies from Eq. (3) is shown in Fig. 6b, with an average value $\mu = 4.43$ eV and a standard deviation $\sigma = 0.54$ eV. We again observe that a Gaussian distribution fits the data remarkably well. In pure W, the formation energy of tetrahedral and octahedral He have been calculated to be in the range of 6.160−6.365 eV and 6.380−6.583 eV, respectively [35−38]. Hence, both the formation and solution energies of He in the HEA are significantly lower than in pure W.

We have also computed the migration barrier for He to jump between two neighboring stable sites. We have analyzed a total of 56 stable barriers, for different He environments. Fig. 7a shows the results. We have again fitted the data to a Gaussian distribution with average $\mu = 0.156$ eV and standard deviation $\sigma = 0.107$ eV. We note that there is a large variety of barriers, with a large standard deviation compared to the average. Fig. 7b shows an example of minimum energy path (MEP) for He migration. Neither the initial nor the final configurations are purely tetrahedral or octahedral
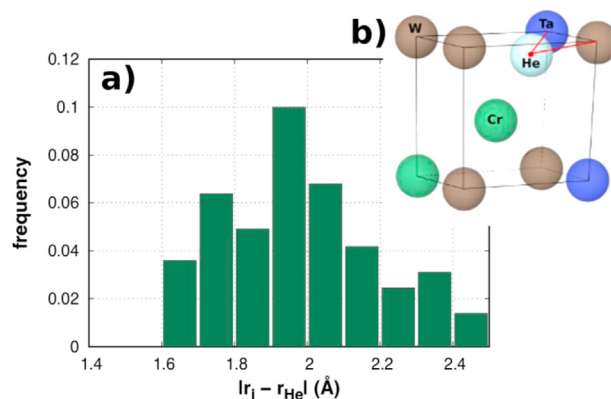

Fig. 4. Formation energies per atom of random HEAs with average atomic composition W35%-Ta35%-V15%-Cr15%.

Fig. 5. a. Distribution of equilibrium distances between the interstitial He (center) and the alloying elements within a radius of 2.5 Å. **b.** Relaxed configuration of an interstitial He showing loss of symmetry.
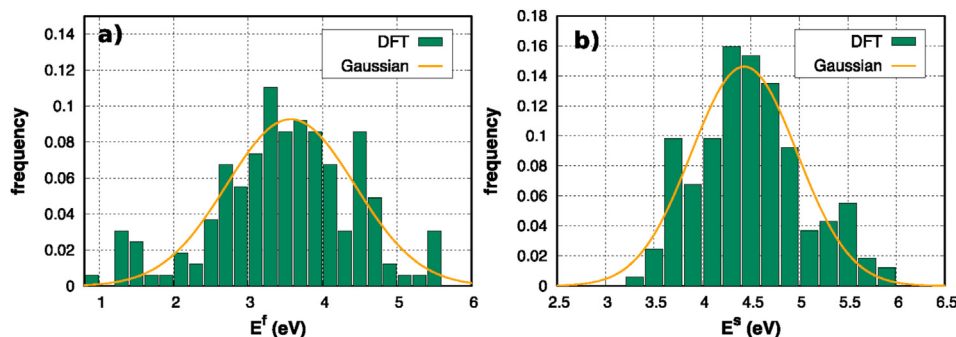
Fig. 6. a. Formation energies of interstitial He in different random HEAs with average atomic composition W35%-Ta35%-V15%-Cr15%. **b.** Solution energy of He in the HEA. Color coding: W-brown, Ta-dark blue, V-yellow, Cr-green, He-light blue. Orange lines in figures **a, b** and **c** show Gaussian distributions of the data.
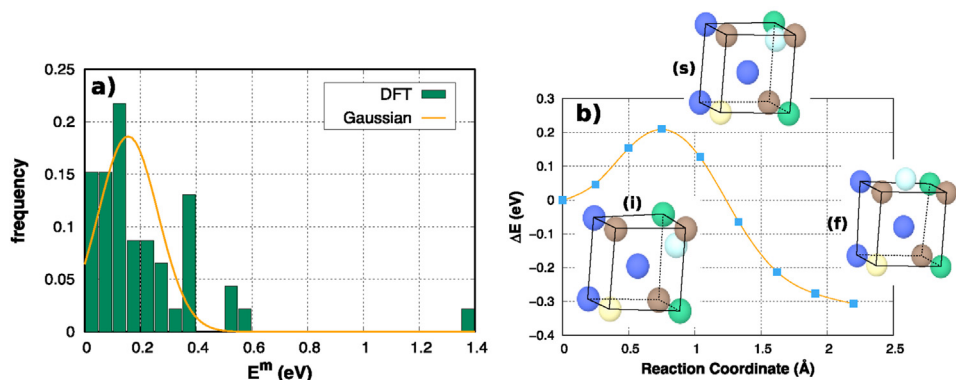

Fig. 7. a. Migration energies distribution for the hop of an interstitial He between two stable sites in a random HEAs with average atomic composition W35%-Ta35%-V15%-Cr15%. **b.** Minimum energy path for the hop of an interstitial He between two stable sites. (i) Denotes the initial, (s) saddle and (f) final configurations. Color coding: W-brown, Ta-dark blue, V-yellow, Cr-green, He-light blue. Orange lines in figures a) shows Gaussian distributions of the data.

sites. The saddle point is fairly at the midpoint in the He MEP, in the vector joining initial and final state.

5. Discussion

It is important to understand the origin of the high radiation resistance to He bubble formation in the HEA. The resistance to loop formation after heavy ion irradiation was attributed to higher recombination probability of self-interstitials and vacancies due to potentially similar defect mobilities [15]. Zhao [22] demonstrated, via first principle calculations, large overlapping regions of interstitial and vacancy formation energies. While these conclusions can assist in understanding the resistance to bubble formation, other information regarding He formation and migration is needed.

To put the data obtained in this work into context, several implications can be drawn from the modeling results when correlated with the experimental data. The average formation energy of interstitial He in the alloy is ~2 times lower than the formation energy in pure W [35]. We also observe that there are sites with low formation energy that will probably lead to deep wells in the potential energy landscape that will behave as strong traps for He, potentially inhibiting its migration. The migration barrier of He from tetrahedral to tetrahedral site in pure W has been reported to be in the range of 0.06−0.081 eV, without and with zero-point energy corrections [36−39]. These values are significantly lower than the average interstitial He migration energy barrier in this alloy (0.156 eV), computed without zero-point energy correction. The rough energy landscape implies that He has a higher tendency than in pure W to quickly find a fairly stable site that can act as a

bubble nuclei, binding with other slowly migrating He atoms or He atoms coming directly from the implantation beam. As He-He binding occurs, cluster diffusivity will decrease further and the propensity for small bubble nucleation will be enhanced. This agrees with the experimental results where bubbles were shown to follow a uniform distribution with no preferential bubble formation on the grain boundaries or a wide distribution of bubble sizes. Such uniform distribution in pure W was only observed under low energy implantation conditions (50 eV) where no W atom displacement (no vacancy generation due to atomic displacement) occurs or at temperature where He-V complex migration is supressed [40]. He-vacancy complexes which are expected to form and have a migration energy that can allow them to migrate, help widen bubble size distribution and preferential He bubble formation on grain boundaries. Those complexes should be of type He_nV_m where n/m is smaller than 1 and are expected to occur when atomic displacement is significant, which depends on the displacement energy threshold [29,37]. Zhao has also reported lower vacancy migration values in this HEA than in pure W and therefore, the vacancy migration is more-significant at this temperature [22]. However, since the diffusivity of He atoms is significantly slower with the presence of deep traps, the formation of He-vacancy complexes might not be as probable as in pure W. This stems from the fact that He-vacancy formation is proportional to the diffusivities of He and vacancy defects with significantly dominant He diffusivity values. He and vacancy concentrations in the matrix also affect the formation of these complexes although deconvolution of concentration and diffusivity factors requires further reaction rate calculations. Therefore, only vacancy migration can

contribute to large bubble formation on the grain boundaries and wide bubble size distribution by combining with migrating He at the grain boundaries. Assuming the latter mechanism is governing large bubble formation at the grain boundaries in the HEA, the absence of these large bubbles and wide bubble distribution in our results should then indicate that relatively-low numbers of vacancies are reaching the grain boundaries. Therefore, the absence of such preferential bubble formation on the grain boundaries or wide bubble size distribution in the HEA can indicate (1) a high migration barrier of He-V complexes, (2) slow migration of He to the grain boundaries (which can bind with migrating vacancies at the grain boundaries or in the grain matrices on its way to the grain boundaries) and/or (3) a higher recombination of vacancies and self-interstitials which has been suggested by the results of Zhao [22] and El-Atwani et al. [15] and which contributes to the overall lower damage in this alloy compared to other studied W grades. Therefore, while the radiation resistance to bubble formation in pure nanocrystalline tungsten and ultrafine conventional alloys is an outcome of the high defect absorption by the grain boundaries (which results in large bubble formation on the grain boundaries), the radiation resistance in the HEA stems from favorable defect properties and matrix chemistry.

Understanding He implantation response and the mechanisms behind the higher irradiation resistance (and the damage plateau observed at high fluences) in this alloy requires coordinated experimental and simulation studies, complimentary to this work, where different atomistic processes such as He-vacancy, vacancy, self-interstitials and He interstitial formation, binding and migration energies as well as defect properties on the grain boundaries are all evaluated and correlated to the irradiation response under different irradiation conditions (i.e. particle energy and temperature).

6. Conclusion

To conclude, the response of nanocrystalline W-Ta-Cr-V HEA alloy is investigated under low energy He implantation at 1223 K. A uniform distribution of small bubbles was observed and bubble damage reached a plateau at high fluences. Unlike pure nanocrystalline W and other studied ultrafine W grades, no preferential bubble formation was observed on the grain boundaries even at one order of magnitude higher fluence where large bubble formation occurred in pure nanocrystalline W. These results suggest higher resistance to fuzz formation and softening in the mechanical response of these alloys. Computation of He formation and migration energies showed ~2 times lower formation energies and 2 times larger migration energies than in pure W, indicating a higher tendency to form a uniform distribution of smaller bubbles. Similar to high energy irradiation, the response of this alloy to He implantation is remarkably better than pure nanocrystalline W and other studied alloys such as W-TiC when considering the overall damage (both grain matrices and grain boundaries). This higher implantation resistance of the HEA, compared to pure W forms, stems from less probable He-vacancy formation and slow migration, slower He diffusion, and enhanced interstitial and vacancy recombination.

CRediT authorship contribution statement

O. El-Atwani: Conceptualization, Investigation, Funding acquisition, Writing - original draft. **A. Alvarado:** Formal analysis, Investigation. **K. Unal:** Formal analysis, Investigation. **S. Fensin:** Validation, Investigation. **J.A. Hinks:** Methodology, Investigation. **G. Greaves:** Methodology, Investigation, Writing - review & editing. **J.K.S. Baldwin:** Resources, Investigation. **S.A. Maloy:** Funding acquisition, Conceptualization. **E. Martinez:** Conceptualization, Investigation, Funding acquisition, Writing - original draft.

Declaration of competing interest

The authors declare that they have no known competing financial interests or personal relationships that could have appeared to influence the work reported in this paper.

Acknowledgements

Appendix A. Supplementary data

Supplementary data to this article can be found online at https://doi.org/10.1016/j.mtener.2020.100599.

Data availability statement

The authors confirm that the data supporting the findings of this study are available within the article [and/or] its supplementary materials.

References

[1] L. Mansur, A. Rowcliffe, R. Nanstad, S. Zinkle, W. Corwin, R. Stoller, Materials needs for fusion, Generation IV fission reactors and spallation neutron sources−similarities and differences, J. Nucl. Mater. 329 (2004) 166−172.

[2] S.J. Zinkle, J.T. Busby, Structural materials for fission & fusion energy, Mater. Today 12 (11) (2009) 12−19.

[3] S.J. Zinkle, G. Was, Materials challenges in nuclear energy, Acta Mater. 61 (3) (2013) 735−758.

[4] B. Wirth, K. Nordlund, D. Whyte, D. Xu, Fusion materials modeling: challenges and opportunities, MRS Bull. 36 (3) (2011) 216−222.

[5] B.D. Wirth, K. Hammond, S. Krasheninnikov, D. Maroudas, Challenges and opportunities of modeling plasma−surface interactions in tungsten using high-performance computing, J. Nucl. Mater. 463 (2015) 30−38.

[6] D. Naujoks, R. Behrisch, Erosion and redeposition at the vessel walls in fusion devices, J. Nucl. Mater. 220 (1995) 227−230.

[7] S.J. Zinkle, L.L. Snead, Designing radiation resistance in materials for fusion energy, Annu. Rev. Mater. Res. 44 (2014) 241−267.

[8] Y. Katoh, L.L. Snead, L.M. Garrison, X. Hu, T. Koyanagi, C.M. Parish, P.D. Edmondson, et al., Response of unalloyed tungsten to mixed spectrum neutrons, J. Nucl. Mater. 520 (2019) 193−207.

[9] G. Federici, A. Zhitlukhin, N. Arkhipov, R. Giniyatulin, N. Klimov, I. Landman, V. Podkovyrov, V. Safronov, A. Loarte, M. Merola, Effects of ELMs and disruptions on ITER divertor armour materials, J. Nucl. Mater. 337 (-339) (2005) 684−690.

[10] V. Philipps, Tungsten as material for plasma-facing components in fusion devices, J. Nucl. Mater. 415 (1) (2011) S2−S9.

[11] J. Knaster, A. Moeslang, T. Muroga, Materials research for fusion, NatPh 12 (5) (2016) 424−434.

[12] S. Kajita, N. Yoshida, R. Yoshihara, N. Ohno, M. Yamagiwa, TEM observation of the growth process of helium nanobubbles on tungsten: nanostructure formation mechanism, J. Nucl. Mater. 418 (1) (2011) 152−158.

[13] V. Sikka, J. Moteff, "Rafting" in neutron irradiated tungsten, J. Nucl. Mater. 46 (2) (1973) 217−219.

[14] F. Sefta, K.D. Hammond, N. Juslin, B.D. Wirth, Tungsten surface evolution by helium bubble nucleation, growth and rupture, Nucl. Fusion 53 (7) (2013), 073015.

[15] O. El-Atwani, N. Li, M. Li, A. Devaraj, J. Baldwin, M.M. Schneider, D. Sobieraj, J.S. Wróbel, D. Nguyen-Manh, S.A. Maloy, Outstanding radiation resistance of tungsten-based high-entropy alloys, Sci. Adv. 5 (3) (2019), eaav2002.

[16] E.P. George, D. Raabe, R.O. Ritchie, High-entropy alloys, Nat. Rev. Mater. (2019) 1.

[17] J.W. Yeh, S.K. Chen, S.J. Lin, J.Y. Gan, T.S. Chin, T.T. Shun, C.H. Tsau, S.Y. Chang, Nanostructured high-entropy alloys with multiple principal elements: novel alloy design concepts and outcomes, Adv. Eng. Mater. 6 (5) (2004) 299−303.

[18] M.-H. Tsai, J.-W. Yeh, High-entropy alloys: a critical review, Mater. Res. Lett. 2 (3) (2014) 107−123.

[19] D.J.M. King, Investigation of High-Entropy Alloys for Use in Advanced Nuclear Applications, 2016.

[20] Y. Zhang, K. Jin, H. Xue, C. Lu, R.J. Olsen, L.K. Beland, M.W. Ullah, S. Zhao, H. Bei, D.S. Aidhy, Influence of chemical disorder on energy dissipation and defect evolution in advanced alloys, J. Mater. Res. 31 (16) (2016).

[21] Y. Zhang, G.M. Stocks, K. Jin, C. Lu, H. Bei, B.C. Sales, L. Wang, L.K. Béland, R.E. Stoller, G.D. Samolyuk, Influence of chemical disorder on energy dissipation and defect evolution in concentrated solid solution alloys, Nat. Commun. 6 (1) (2015) 1−9.

[22] S. Zhao, Defect properties in a VTaCrW equiatomic high entropy alloy (HEA) with the body centered cubic (bcc) structure, J. Mater. Sci. Technol. 44 (2020) 133−139.

[23] G. Greaves, A. Mir, R. Harrison, M. Tunes, S. Donnelly, J. Hinks, New microscope and ion Accelerators for materials Investigations (MIAMI-2) system at the University of Huddersfield, Nucl. Instrum. Methods Phys. Res. Sect. A Accel. Spectrom. Detect. Assoc. Equip. 931 (2019) 37−43.

[24] J.F. Ziegler, M.D. Ziegler, J.P. Biersack, SRIM−The stopping and range of ions in matter (2010), Nucl. Instrum. Methods Phys. Res. Sect. B Beam Interact. Mater. Atoms 268 (11) (2010) 1818−1823.

[25] P. Jung, in: H. Ullmaier (Ed.), Atomic Defects in Metals (Landolt-Bornstein New Series III/25), Springer, Berlin, 1991.

[26] O. El-Atwani, J. Nathaniel, A. Leff, B. Muntifering, J. Baldwin, K. Hattar, M. Taheri, The role of grain size in He bubble formation: implications for swelling resistance, J. Nucl. Mater. 484 (2017) 236−244.

[27] O. El Atwani, K. Unal, W.S. Cunningham, S. Fensin, J. Hinks, G. Greaves, S. Maloy, In-situ helium implantation and TEM investigation of radiation

[28] tolerance to helium bubble damage in equiaxed nanocrystalline tungsten and ultrafine tungsten-TiC alloy, Materials 13 (3) (2020) 794.

[28] O. El-Atwani, J. Hinks, G. Greaves, J. Allain, S. Maloy, Grain size threshold for enhanced irradiation resistance in nanocrystalline and ultrafine tungsten, Mater. Res. Lett. (2017) 1−7.

[29] D. Reed, A review of recent theoretical developments in the understanding of the migration of helium in metals and its interaction with lattice defects, Radiat. EIT. 31 (3) (1977) 129−147.

[30] O. El-Atwani, J. Hinks, G. Greaves, S. Gonderman, T. Qiu, M. Efe, J.P. Allain, In-situ TEM observation of the response of ultrafine-and nanocrystalline-grained tungsten to extreme irradiation environments, Sci. Rep. 4 (2014) 4716.

[31] O. El-Atwani, W. Cunningham, E. Esquivel, M. Li, J. Trelewicz, B. Uberuaga, S. Maloy, In-situ irradiation tolerance investigation of high strength ultrafine tungsten-titanium carbide alloy, Acta Mater. 164 (2019) 547−559.

[32] M. Li, M. Kirk, P. Baldo, D. Xu, B. Wirth, Study of defect evolution by TEM with in situ ion irradiation and coordinated modeling, Philos. Mag. 92 (16) (2012) 2048−2078.

[33] W.S. Cunningham, J.M. Gentile, O. El-Atwani, C.N. Taylor, M. Efe, S.A. Maloy, J.R. Trelewicz, Softening due to grain boundary cavity formation and its competition with hardening in helium implanted nanocrystalline tungsten, Sci. Rep. 8 (1) (2018) 2897.

[34] B. Muntifering, S.J. Blair, C. Gong, A. Dunn, R. Dingreville, J. Qu, K. Hattar, Cavity evolution at grain boundaries as a function of radiation damage and thermal conditions in nanocrystalline nickel, Mater. Res. Lett. (2015) 1−8.

[35] C. Becquart, C. Domain, Ab initio calculations about intrinsic point defects and He in W, Nucl. Instrum. Methods Phys. Res. Sect. B Beam Interact. Mater. Atoms 255 (1) (2007) 23−26.

[36] C.S. Becquart, C. Domain, Migration energy of He in W revisited by ab initio calculations, Phys. Rev. Lett. 97 (19) (2006) 196402.

[37] C. González, R. Iglesias, Migration mechanisms of helium in copper and tungsten, JMatS 49 (23) (2014) 8127−8139.

[38] A.J. Samin, A physics-based machine learning study of the behavior of interstitial helium in single crystal W−Mo binary alloys, J. Appl. Phys. 127 (17) (2020) 175904.

[39] A. Debelle, M. Barthe, T. Sauvage, R. Belamhawal, A. Chelgoum, P. Desgardin, H. Labrim, Helium behaviour and vacancy defect distribution in helium implanted tungsten, J. Nucl. Mater. 362 (2−3) (2007) 181−188.

[40] O. El-Atwani, K. Hattar, J. Hinks, G. Greaves, S. Harilal, A. Hassanein, Helium bubble formation in ultrafine and nanocrystalline tungsten under different extreme conditions, J. Nucl. Mater. 458 (2015) 216−223.